

## Strong evidence for quasifission in asymmetric reactions forming $^{202}\text{Po}$

R. Rafiei, R. G. Thomas,\* D. J. Hinde, M. Dasgupta, C. R. Morton, L. R. Gasques, M. L. Brown, and M. D. Rodriguez

*Department of Nuclear Physics, Research School of Physical Sciences and Engineering,*

*The Australian National University, Canberra, ACT 0200, Australia*

(Received 27 November 2007; published 13 February 2008)

Fission fragment mass-angle correlations and mass ratio distributions have been measured for the reactions  $^{16}\text{O} + ^{186}\text{Os}$ ,  $^{24}\text{Mg} + ^{178}\text{Hf}$ ,  $^{34}\text{S} + ^{168}\text{Er}$ , and  $^{48}\text{Ti} + ^{154}\text{Sm}$ , forming the  $^{202}\text{Po}$  composite nucleus, at near barrier energies. Systematic analysis based on the expected dependence of the variance of the mass distribution on the angular momentum and temperature of the compound nucleus indicate that the two lighter systems evolve through true compound nucleus fission. Evidence of quasifission was observed for the two most mass-symmetric reactions, through strong mass-angle correlations for the  $^{48}\text{Ti} + ^{154}\text{Sm}$  reaction and a broadened mass ratio distribution for the  $^{34}\text{S} + ^{168}\text{Er}$  reaction. Furthermore, the increase in mass width at near barrier energies shows the influence of the alignment of statically deformed target nuclei.

DOI: [10.1103/PhysRevC.77.024606](https://doi.org/10.1103/PhysRevC.77.024606)

PACS number(s): 25.70.Jj, 25.85.Ge

### I. INTRODUCTION

Experimental efforts aiming at the formation of superheavy nuclei followed the prediction, nearly half a century ago, of an island of super-heavy nuclei with enhanced stability due to shell effects [1,2]. Evidence of the formation of long-lived isotopes of elements with  $Z = 113$  [3], 114 [4], 116 [5], and 118 [6] have recently energised experimental efforts. Such experiments are extremely challenging as the formation of heavy/superheavy evaporation residues (ER) is heavily suppressed not only by equilibrium fission, but also by a nonequilibrium process called quasifission (QF) [7–10]. Following the capture of the projectile and target nuclei, the system may reseparate prematurely, not forming a true compound nucleus (CN). Such events represent the transition between deep-inelastic collisions (DIC) and complete fusion. In DIC the entrance channel mass-asymmetry is preserved, but there can be large dissipation of kinetic energy and angular momentum [11]. CN formation, in contrast, is characterized by equilibration of all degrees of freedom, and hence complete loss of identity of the entrance channel. Intermediate between DIC and CN fission, QF has full energy dissipation but incomplete drift toward the energetically favoured mass-symmetric configuration [12].

The experimental problem is to identify those variables that hinder CN formation. This can be addressed by measuring the characteristics of the QF events. Properties of the entrance channel appear to play a major role in the reaction dynamics of QF, in particular the entrance channel mass-asymmetry (closely related to the product of the projectile and target atomic numbers— $Z_p Z_t$ ), and the deformation of the colliding nuclei [7–9,13,14]. Microscopic effects such as shell closure and neutron excess are also reported to influence the probability of QF [15,16]. While initial measurements of QF were focused on heavy composite nuclei, more recent experimental results, as described in the next two paragraphs, have indicated

an unexpected shift in the onset of quasifission toward lighter composite nuclei.

Early experimental evidence for QF included the observation of broadened mass distributions for the fission-like fragments, and the existence of a strong correlation between fragment mass and emission angle, associated with the short timescale of QF [12,17,18]. Measurements reported in Ref. [17], using beams of  $^{208}\text{Pb}$  on targets with  $26 \leq A \leq 64$ , followed later by those of Refs. [12,18] using beams of  $^{238}\text{U}$  on targets ranging from  $^{16}\text{O}$  to  $^{89}\text{Y}$ , showed broadened mass distributions and strong mass-angle correlations for  $A > 27$ . The influence of the entrance channel mass-asymmetry on the fusion process for systems forming  $^{243,249}\text{Md}$  showed incomplete relaxation of mass for the more mass-symmetric entrance-channel [19]. Another distinct experimental signature of QF is the large angular anisotropy of the fission fragments [20,21]. Large deviations of angular anisotropies from the predictions of the transition state model (TSM) [22] for compound nucleus fission were shown in Refs. [20,21] for reactions of  $^{24}\text{Mg}$  and heavier projectiles with  $^{208}\text{Pb}$  targets, and interpreted as showing the presence of QF in these systems.

Experimental evidence for the influence of nuclear orientation on QF was first shown in Refs. [23,24]. Unusually large anisotropies were seen for  $^{16}\text{O} + ^{238}\text{U}$  at sub-barrier energies, and were interpreted as enhancement of the probability of QF for near-tip collisions with the prolate deformed target nucleus, demonstrating the existence of QF for  $Z_p Z_t$  far less than the threshold value of 1600 predicted by earlier dynamical models [7]. Similar observations were made by Refs. [25,26] using light projectiles ranging from  $^7\text{Li}$  to  $^{16}\text{O}$  on a range of actinide targets, confirming the effect of deformation on QF. However, measurements of ER cross sections for the  $^{16}\text{O} + ^{238}\text{U}$  reaction showed that CN formation is still present at sub-barrier energies for this reaction [27]. Severe inhibition of ER cross sections for  $^{60,64}\text{Ni} + ^{154}\text{Sm}$  at sub-barrier energies was reported in Refs. [15,28], showing the dominance of QF for capture on the tip of a deformed target nucleus, for a reaction with a heavy projectile.

The presence of QF has also been found, perhaps surprisingly, for less fissile, asymmetric reactions, forming systems

\*Permanent address: Bhabha Atomic Research Centre, Mumbai, India.

TABLE I. Key properties of the four studied systems, all of which form the composite nucleus  $^{202}\text{Po}$ .  $V_b$  is the average capture barrier in the center-of-mass frame.  $\beta_2$  is the static quadrupole deformation of the target, inferred from the electric quadrupole transition probability from the ground to the first excited  $2^+$  state [33].  $\alpha$  is the entrance-channel mass asymmetry ( $=\frac{A_t - A_p}{A_t + A_p}$ ).  $Z_p Z_t$  is the product of the projectile and target atomic numbers, respectively.

Reaction	$V_b$ (MeV)	$\beta_2$	$\alpha$	$Z_p Z_t$
$^{16}\text{O} + ^{186}\text{Os}$	71.0 <sup>a</sup>	0.20	0.84	608
$^{24}\text{Mg} + ^{178}\text{Hf}$	100.6 <sup>b</sup>	0.28	0.76	864
$^{34}\text{S} + ^{168}\text{Er}$	123.1 <sup>a</sup>	0.34	0.66	1088
$^{48}\text{Ti} + ^{154}\text{Sm}$	150.3 <sup>b</sup>	0.34	0.53	1364

<sup>a</sup>Experimental values.

<sup>b</sup>Scaled values (see Sec. III B).

as light as  $^{216}\text{Ra}$  and  $^{220}\text{Th}$ , both populated via a number of entrance channels varying in mass-asymmetry. For  $^{216}\text{Ra}$ , reduction in the evaporation residue cross sections [29] and broadened mass distributions [29,30] were observed for the more symmetric combinations. The mass-asymmetry dependence of QF is also strongly seen in the  $^{220}\text{Th}$  system where substantial reductions in ER cross sections were demonstrated for reactions involving projectiles of  $^{40}\text{Ar}$  and heavier [31]. Incomplete mass relaxation was also observed in the fragment mass distributions for projectiles of  $^{34}\text{S}$  and heavier [32]. For each of these relatively light systems it becomes apparent that there exists a critical target-projectile mass-asymmetry or charge product which marks the onset of QF. A systematic investigation is imperative to understand the entrance channel conditions governing the dynamics of the QF process for light systems. To address this problem, mass distributions and mass-angle correlations of fission-like fragments are measured for four different entrance channel combinations, namely  $^{16}\text{O} + ^{186}\text{Os}$ ,  $^{24}\text{Mg} + ^{178}\text{Hf}$ ,  $^{34}\text{S} + ^{168}\text{Er}$ , and  $^{48}\text{Ti} + ^{154}\text{Sm}$ , all forming the  $^{202}\text{Po}$  composite nucleus. Their properties are listed in Table I.

## II. EXPERIMENTAL SETUP AND ANALYSIS PROCEDURE

The experiments were carried out at the Australian National University, using beams from the 14UD tandem electrostatic accelerator. For all four systems, pulsed beams of full width at half maximum  $\sim 1$  ns, with separations of 106–533 ns, were incident on isotopically enriched targets, details of which are listed in Table II. The targets were mounted on a target ladder oriented at  $45^\circ$  to the beam axis ( $30^\circ$  for the  $^{48}\text{Ti} + ^{154}\text{Sm}$  measurements), thus minimizing the energy loss of the fission fragments and eliminating the shadowing of the detectors by the target ladder.

Fission fragments were detected using two large-area ( $28.4 \times 35.7 \text{ cm}^2$ ) position sensitive multiwire proportional counters (MWPCs), which for most measurements were arranged as depicted in Fig. 1. The detectors provided a position resolution of less than 1 mm and a coverage of  $77^\circ$  in scattering angle in both front and rear hemispheres. Reactions of  $^{16}\text{O}$ ,  $^{24}\text{Mg}$ , and  $^{34}\text{S}$  used this detector configuration, with

TABLE II. Laboratory beam energy ranges (inclusive) and thickness ( $t$ ) of the target and backing materials used in the measurements.

Projectile	$E_{\text{lab}}$ (MeV)	Target $t$ ( $\text{mg cm}^{-2}$ )	Backing $t$ ( $\text{mg cm}^{-2}$ )
$^{16}\text{O}$	74–105	$^{186}\text{Os}$ 0.020	C 0.025
$^{24}\text{Mg}$	106–144	$^{178}\text{Hf}$ 0.040	Al 0.030
$^{34}\text{S}$	141–174	$^{168}\text{Er}$ 0.100	Al, C 0.030, 0.015
$^{48}\text{Ti}$	198–235	$^{154}\text{Sm}$ 0.030	C 0.018

the front detector centered at scattering angle  $\theta = 45^\circ$  and at azimuthal angle  $\phi = 90^\circ$ ; the rear detector was centered at  $(\theta, \phi) = (135^\circ, 270^\circ)$ . For reactions induced by  $^{48}\text{Ti}$ , the geometry of the back detector was changed to  $(\theta, \phi) = (90^\circ, 270^\circ)$  to cater for the increased forward focusing of the fission fragments. The closest point of each fission detector was 18.0 cm from the target. All target backings faced downstream (facing the front detector) to eliminate the energy loss of the beam through the backing, and minimise that of the slower fragments directed at the rear detector. A pair of silicon surface barrier detectors (monitors), placed at  $\theta = \pm 22.5^\circ$ , were used to measure the elastically scattered beam particles for normalisation and absolute cross-section determination.

The center-foil of each MWPC recorded the timing and energy-loss signals, while position information was obtained from the wire grids using the delay-line read out technique. For position calibration, the full image of both front and rear detectors was captured separately by operating in singles mode. Channel numbers corresponding to the physical edges of each detector were then converted to (x,y) positions. To minimise counting rates, events in the front counter were

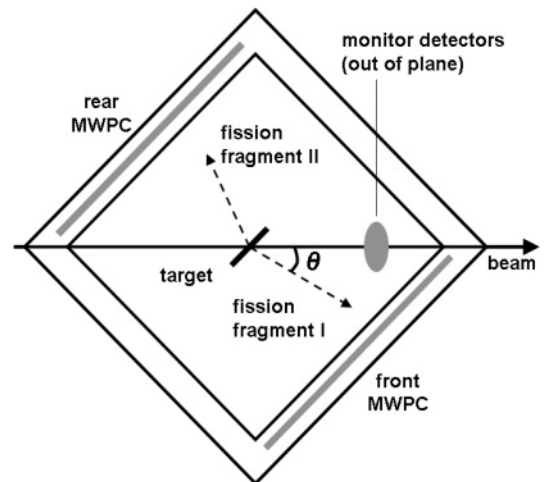


FIG. 1. Configuration of the MWPCs for the detection of binary fission fragments in the  $^{16}\text{O}$ ,  $^{24}\text{Mg}$ , and  $^{34}\text{S}$  induced reactions. Details are provided in the text.

only recorded when in coincidence with the rear detector. The  $(x, y)$  positions in each detector were then converted to  $\theta$  and  $\phi$ . The accuracy of the angular calibrations were confirmed by comparing measured elastic folding angles with their calculated values. The former were measured at sub-barrier energies for heavy projectiles in order to ensure all detected events were pure Rutherford scattering.

The  $(\theta, \phi)$  information in combination with the time-of-flight information, allowed the reconstruction of the laboratory frame fragment velocities  $(\vec{v}_{1\text{lab}}, \vec{v}_{2\text{lab}})$ . Timing calibrations involved the optimisation of two parameters,  $t_o$  and  $\delta t_o$ .  $t_o$  is the time shift between the RF reference signal and the arrival of the beam pulse at the target, used to calculate the reaction time-zero. By its very nature  $t_o$  is energy dependent and is adjusted at each energy making use of binary reaction kinematics as described below. The velocity of the fissioning system in the beam direction ( $V_{\parallel}$ ) can be determined from the measured fragment velocities through the relation [24]

$$V_{\parallel} = \frac{v_{1\text{lab}} v_{2\text{lab}} \sin(\theta_1 + \theta_2)}{v_{1\text{lab}} \sin \theta_1 + v_{2\text{lab}} \sin \theta_2}, \quad (1)$$

where  $\theta_1$  and  $\theta_2$  are the scattering angles of the binary fragments 1 and 2, respectively. At the near barrier energies used, preequilibrium emission is expected to be negligible, thus  $V_{\parallel}$  is expected to match the calculated center-of-mass velocity  $V_{\text{c.m.}}$ .  $t_o$  was adjusted such that the  $\frac{V_{\parallel}}{V_{\text{c.m.}}}$  distribution peaks at unity for all four reactions studied.  $\delta t_o$ , which is independent of beam energy, is a constant electronic delay between the two detectors, obtained by requiring the fission fragment mass ratio distribution to be reflection symmetric about 0.5 for those systems with no observed mass-angle correlation, or symmetric about 0.5 at  $\theta_{\text{c.m.}} = 90^\circ$  for the  $^{48}\text{Ti}$  induced reactions where a mass-angle correlation was observed.

With the application of kinematic transformations, the center-of-mass velocity vectors,  $\vec{v}_{1\text{c.m.}}$  of the fragment with mass  $m_1$ , and  $\vec{v}_{2\text{c.m.}}$  of the fragment with mass  $m_2$ , were obtained. Corrections for the fragment energy losses through the target material and target backing were included in the data analysis, with the assumption that reactions occur on average at the target midpoint. Using the conservation of linear momentum, the mass ratio was then obtained from the relation

$$M_R = \frac{m_2}{m_1 + m_2} = \frac{\vec{v}_{1\text{c.m.}}}{\vec{v}_{1\text{c.m.}} + \vec{v}_{2\text{c.m.}}}. \quad (2)$$

Evaporation residue cross sections for the  $^{16}\text{O} + ^{186}\text{Os}$  reaction were separated from beam particles using a compact velocity filter, on a rotating arm, in a 2 m diameter scattering chamber. The identification of the ERs was achieved by energy and time-of-flight measurements in a large area Si detector. The experimental methods were identical to those described in Ref. [34].

### III. RESULTS AND INTERPRETATION

#### A. Mass-angle correlations and mass ratio distributions

The wide angular acceptance of the detectors allowed the extraction of broad-ranging mass-angle correlations. Exam-

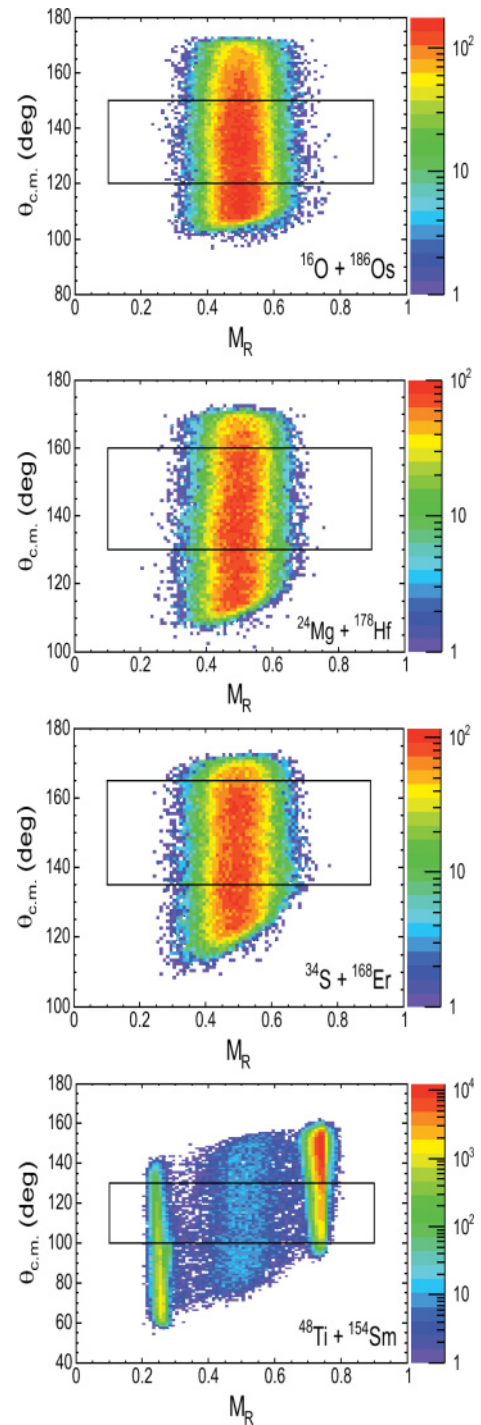


FIG. 2. (Color online) Density plots of mass ratio vs center-of-mass angle for the four systems leading to  $^{202}\text{Po}$ . The data shown are for  $\frac{E_{\text{c.m.}}}{V_b} \approx 1$ , corresponding to  $E_{\text{c.m.}} = 72.6, 102.1, 126.0,$  and  $156.8$  MeV for the  $^{16}\text{O}$ ,  $^{24}\text{Mg}$ ,  $^{34}\text{S}$ , and  $^{48}\text{Ti}$  induced reactions, respectively. The density axis is labeled on the right of each figure.

ples are shown in Fig. 2, where the center-of-mass angle has been plotted against the mass ratio for each of the four systems studied, and displayed in order of decreasing mass-asymmetry. Uniformity in the azimuthal angle coverage was maintained by taking only a fixed coverage of  $\Delta\phi = 70^\circ$ . As a result, the

number of counts in the mass-angle correlations is proportional to the differential cross section  $\frac{d^2\sigma}{dM_R d\theta}$ . The plots correspond to beam energies close to the capture barrier energies, where the mass-angle correlation, if present, is magnified due to the increasing presence of QF in the case of deformed target nuclei [24]. For  $^{48}\text{Ti} + ^{154}\text{Sm}$  the deep inelastic groups on the left and right hand sides of the fission region are visible. To generate mass ratio spectra unbiased by the geometrical limitations of the detectors, rectangular gates, as seen in Fig. 2, have been imposed, such that only the region within these gates is used to produce the mass ratio spectra, examples of which are given in Fig. 3. The dimensions of the gate in  $\theta_{c.m.}$  were different for each system due to varying reaction dynamics, and in the case of  $^{48}\text{Ti} + ^{154}\text{Sm}$ , the added effect of a different detector configuration.

Two mass ratio spectra are shown in Fig. 3 for each reaction, one at an energy well-above the barrier and one at or below the barrier. In the case of the  $^{48}\text{Ti} + ^{154}\text{Sm}$  reaction an additional gate was placed on the ratio of the measured kinetic energy of the fissioning fragments to the mass-asymmetry dependent Viola systematics, as in Ref. [35]. This gate covered the range of 0.8–1.2 and reduced the elastic and deep-inelastic contributions without affecting the QF mass distributions. The mass distributions can be most simply characterized by a Gaussian function, where the standard deviation,  $\sigma_M$ , defines the width of the mass ratio distribution of the fission fragments. In the reactions with  $^{16}\text{O}$ ,  $^{24}\text{Mg}$ , and  $^{34}\text{S}$ , a small fraction of heavy fission fragments ( $M_R > 0.7$ ) were lost through falling below timing thresholds. The effect on the mass widths was less than the statistical uncertainties. The elastic scattering peak for the reaction of  $^{34}\text{S} + ^{168}\text{Er}$  at  $E_{c.m.} = 119.4$  MeV was used to estimate the effect of the instrumental resolution on the mass width. This effect was found to be less than 1%, and being much smaller than statistical uncertainties, was neglected.

The mass-angle plots in Fig. 2 for the reactions  $^{16}\text{O} + ^{186}\text{Os}$ ,  $^{24}\text{Mg} + ^{178}\text{Hf}$ , and  $^{34}\text{S} + ^{168}\text{Er}$  show no significant dependence of mass ratio on the center-of-mass angle. However, the system  $^{48}\text{Ti} + ^{154}\text{Sm}$  shows evidence of a significant correlation between mass ratio and  $\theta_{c.m.}$ . Because of the detection of both fission fragments in the detectors, each point shown in Fig. 2 has a corresponding point at an angle  $\pi - \theta_{c.m.}$ , with mass ratio  $1 - M_R$ . For the lighter projectiles, the mass distributions do not extend to  $\theta_{c.m.} = 90^\circ$ , thus applying this transformation would result in a mass-angle distribution with a gap. However, for the  $^{48}\text{Ti} + ^{154}\text{Sm}$  reaction, the data extend forward of  $\theta_{c.m.} = 90^\circ$ , and thus a continuous distribution can be generated. This is shown in Fig. 4, where the data below the white line have been generated from the data above by applying the above transformation. The mass-angle correlation is seen more clearly here, as the shift in mean mass is doubled compared with Fig. 2. The correlation suggests a strong contribution from quasifission for all mass-splits. This agrees with the correlations seen for  $^{48,50}\text{Ti} + ^{166,168,170}\text{Er}$  reactions, measured [13,32] by two different techniques. However, it does not agree with the measurements presented in Ref. [16] for the reaction  $^{48}\text{Ca} + ^{154}\text{Sm}$ , very similar to the  $^{48}\text{Ti} + ^{154}\text{Sm}$  reaction measured in this work. There, only the most asymmetric mass-splits showed a mass-angle correlation (or angular asymmetry

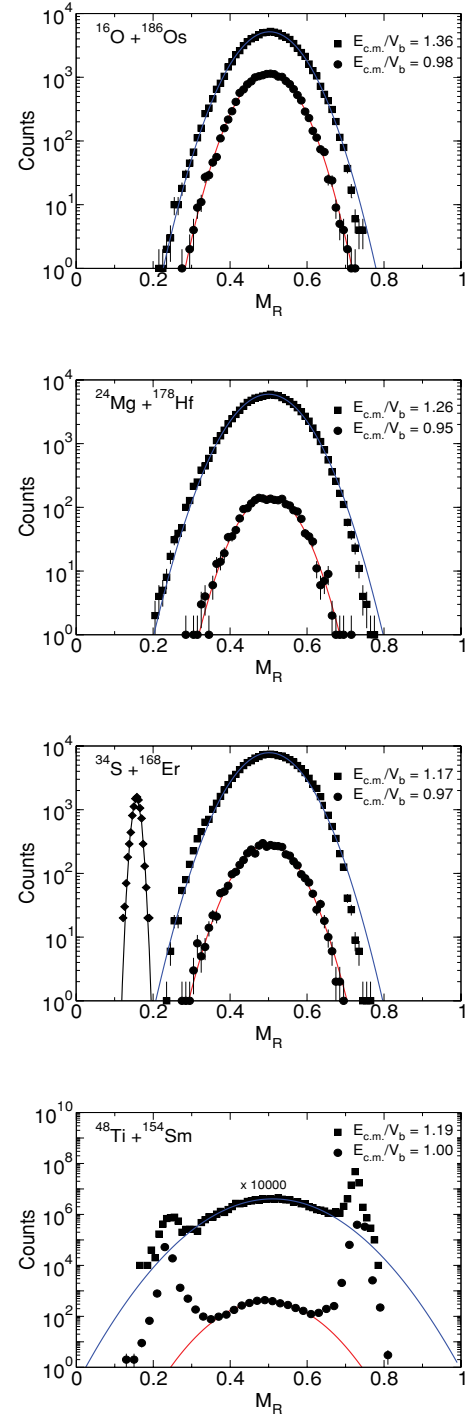


FIG. 3. (Color online) Mass ratio distributions for the four systems which lead to the  $^{202}\text{Po}$  nucleus in order of increasing mass-symmetry. Overlaid on each distribution is a best fit Gaussian function (see text). Also shown on the plot of  $^{34}\text{S} + ^{168}\text{Er}$  is the elastic scattering peak, showing the instrumental resolution.

about  $90^\circ$ ). The reasons for this difference might include the different  $Z_p Z_t$ , the less fissile CN, or different experimental conditions. As the different behavior affects the interpretation of the mass-splits associated with QF, further investigation is required.

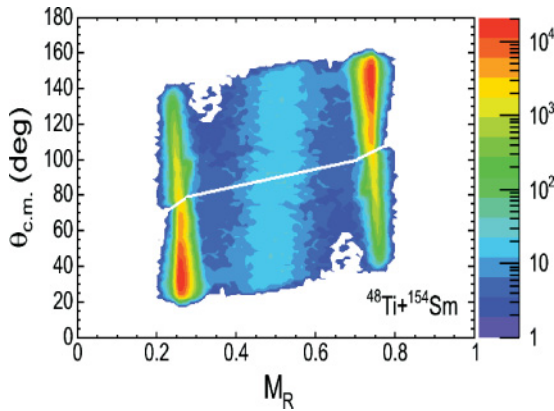


FIG. 4. (Color online) Contour plot for the  $^{48}\text{Ti} + ^{154}\text{Sm}$  reaction. The distribution is transposed across the white line to show the correlation between mass ratio and  $\theta_{\text{c.m.}}$  over a wider angular range (see text).

**B. Dependence of  $\sigma_M$  on  $E^*$  and  $\langle J^2 \rangle$**

It is expected that for an equilibrated CN, the variance of the fission-like mass distribution,  $\sigma_M^2$ , depends linearly on the temperature ( $T$ ), and the mean square angular momentum ( $\langle J^2 \rangle$ ) [36–39]. For all four systems the mass widths are plotted against the compound nucleus excitation energy ( $E^*$ ) in Fig. 5. The monotonic rise in  $\sigma_M$  as a function of  $E^*$  is immediately apparent for all but the most mass-symmetric reaction. This rise need not only be related to  $E^*$ , as increasing beam energy is also associated with increasing  $\langle J^2 \rangle$ .

To account for the dependence of  $\sigma_M$  on the angular momentum brought in by the projectile, the variation of  $\langle J^2 \rangle$  as a function of the excitation energy of the compound system for the four systems must be calculated. The  $\langle J^2 \rangle$  values can be determined from calculations which reproduce experimental fusion excitation functions [40]. The coupled channels code CCFULL [41] was used for the calculations, including rotational couplings in the target nuclei. To avoid numerical

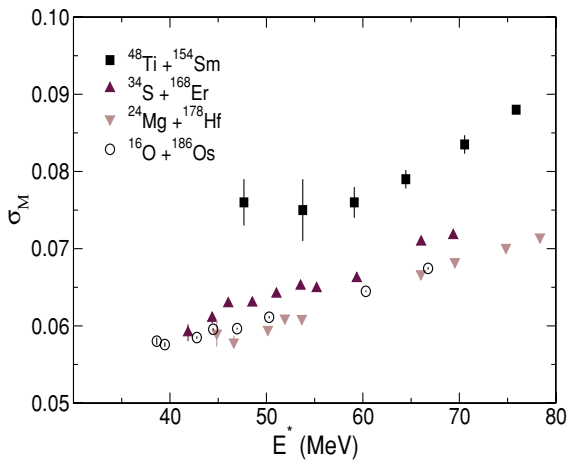


FIG. 5. (Color online) Dependence of the fission fragment  $\sigma_M$  on the compound nucleus excitation energy for four different entrance channels forming  $^{202}\text{Po}$ . A monotonic rise in  $\sigma_M$  with increasing excitation energies is observed for all reactions, except the  $^{48}\text{Ti} + ^{154}\text{Sm}$  reaction.

problems in the code, a deep Woods-Saxon nuclear potential of 250 MeV was used for all four reactions. For the  $^{16}\text{O} + ^{186}\text{Os}$  and  $^{34}\text{S} + ^{168}\text{Er}$  [42] reactions, both ER and fission cross sections were available, allowing determination of the capture excitation functions. These data allowed the average capture barrier energies to be determined, as given in Table I. For the other reactions, the barrier energies were determined by scaling from the  $^{34}\text{S} + ^{168}\text{Er}$  reaction using the Coulomb parameter  $Z_p Z_t / (A_p^{1/3} + A_t^{1/3})$ , and are also given in Table I. A diffuseness parameter of 1.2 fm gave a satisfactory description of the measured capture cross sections for the  $^{16}\text{O}$  and  $^{34}\text{S}$  induced reactions, and was used also for the other reactions. Such large diffusenesses may result from the presence of deep inelastic reactions [43], and do not necessarily reflect the diffuseness of the nuclear potential. The variation of  $\langle J^2 \rangle$  as a function of the excitation energy of the compound system for the four systems is shown in Fig. 6. The  $J$  values populated for the four systems in the energy range studied are almost always less than the critical angular momentum ( $64\hbar$ ) at which the liquid drop fission barrier [44] is reduced to 1 MeV. The probability for fast fission contributing to the measured fission yield is thus negligible [45]. It is seen in Fig. 6 that for the two lighter reactions, induced by  $^{16}\text{O}$  and  $^{24}\text{Mg}$ , the calculated  $\langle J^2 \rangle$  values are very similar; this similarity is reflected in their mass widths shown in Fig. 5. This behavior suggests a similarity in the reaction dynamics of these two systems, and in view of the light projectiles, suggests compound nucleus fission. The similarity is most apparent at an excitation energy just below 70 MeV, where the  $\langle J^2 \rangle$  for the two systems match.

If the fission for all reactions proceeded by the compound nucleus mechanism, it would be expected that they could all be described by a single parametrization. The dependence of  $\sigma_M^2$  on  $E^*$  and  $\langle J^2 \rangle$  has been taken to follow the relation [39]

$$\sigma_M^2 = \nu T + \mu \langle J^2 \rangle, \tag{3}$$

where  $\nu$  and  $\mu$  are here treated as fitting parameters. For compound nucleus fission,  $T$  is the average temperature at

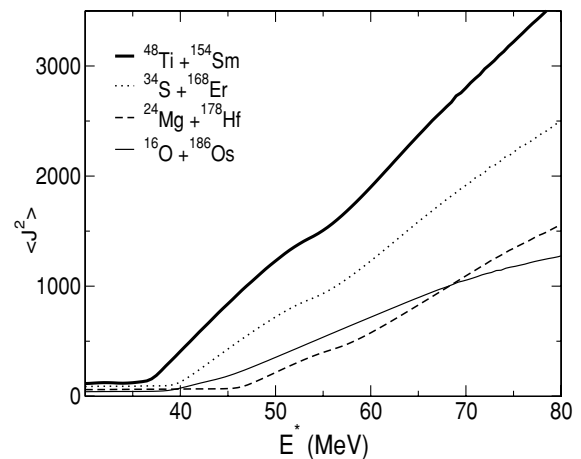


FIG. 6. Calculated dependence of  $\langle J^2 \rangle$  on the excitation energy of the compound system for the four reactions (see text).

the saddle point [16], estimated as

$$T = \sqrt{\frac{E_x}{a}}, \quad (4)$$

where  $a$  is the level density parameter taken as  $a = \frac{A_{CN}}{10}$ , and  $A_{CN}$  is the compound nucleus mass.  $E_x$  is the average excitation energy at the saddle point, given by

$$E_x = E^* - B_{\text{fission}} - E_{\text{rot}} - E_{\text{pre}}, \quad (5)$$

where  $B_{\text{fission}}$  is the fission barrier at the average angular momentum and  $E_{\text{rot}}$  is the average rotational energy at the equilibrium deformation, both calculated using the Sierk model [44].  $E_{\text{pre}}$  is the energy carried away by prefission neutrons, estimated empirically following Ref. [46].

The approach to determine the coefficients  $\nu$  and  $\mu$  in Eq. (3) initially followed that taken by Ref. [16], where the data for the reactions  $^{16}\text{O} + ^{186}\text{W}$  and  $^{48}\text{Ca} + ^{154}\text{Sm}$  at  $E^* \geq 50$  MeV were used. This approach is based on the assumption that these two reactions proceed through true CN fission. The  $^{16}\text{O} + ^{186}\text{Os}$  and  $^{48}\text{Ti} + ^{154}\text{Sm}$  reactions, having matching entrance-channel mass-asymmetry values, were initially used in the fitting procedure. The Levenberg-Marquardt nonlinear least squares fitting technique [47] was used in calculating the  $\nu$  and  $\mu$  constants by minimizing  $\chi^2$ , with the square of the standard errors obtained from the diagonal terms of the covariance matrix. Figure 7 shows the experimental  $\sigma_M$  of Fig. 5 together with the calculated  $\sigma_M$  from the best-fitting  $\nu$  and  $\mu$  parameters [ $\nu = (2.97 \pm 0.10) \times 10^{-3}$ ,  $\mu = (1.23 \pm 0.07) \times 10^{-6}$ ] substituted into Eq. (3). As can be seen, the calculated values fail to reproduce the experimental mass widths in all four reactions. This contrasts with Ref. [16], where a good fit was obtained.

We now make the other extreme assumption, that only the fission for the  $^{16}\text{O} + ^{186}\text{Os}$  and  $^{24}\text{Mg} + ^{178}\text{Hf}$  reactions result from formation of a true CN. For these reactions, our data extend down to  $E^* \approx 40$  MeV, close to the capture barriers. Here, the fact that lower partial waves may result in ER formation and not fission must be considered. Figure 8

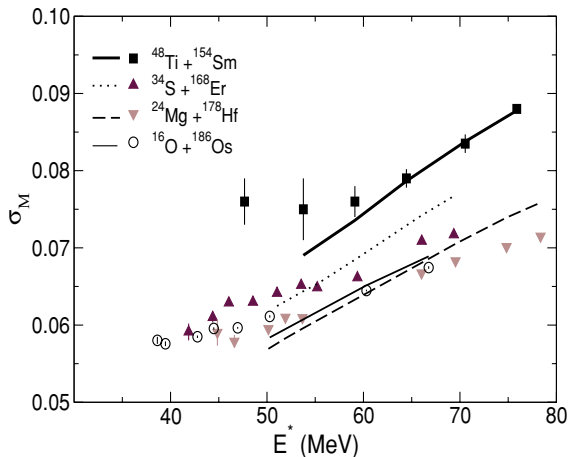


FIG. 7. (Color online) The experimental values for the four reactions (as in Fig. 5) compared with calculations using parameters obtained by simultaneously fitting the  $^{16}\text{O}$  and  $^{48}\text{Ti}$  induced reactions using Eq. (3).

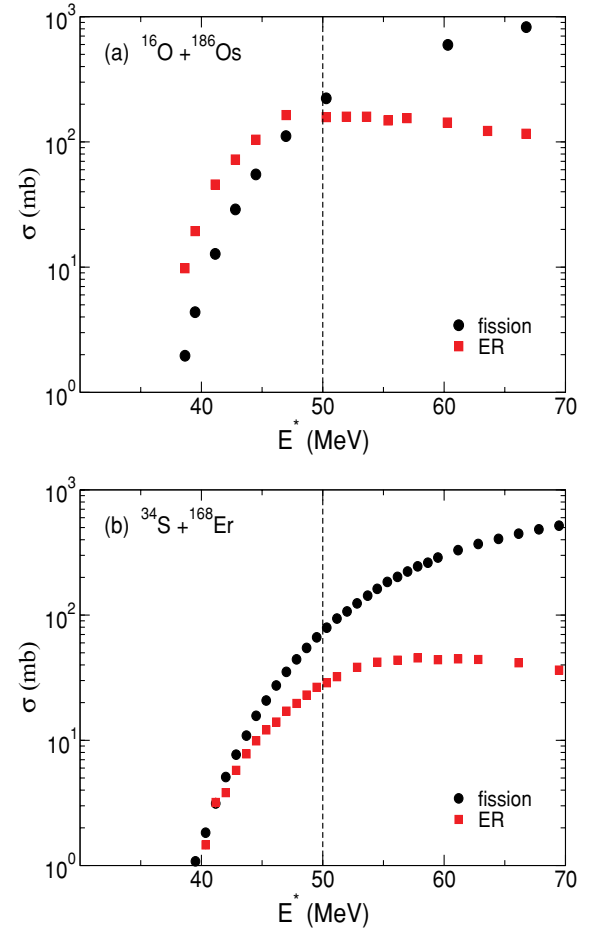


FIG. 8. (Color online) Fission and evaporation residue excitation functions for the reactions (a)  $^{16}\text{O} + ^{186}\text{Os}$  and (b)  $^{34}\text{S} + ^{168}\text{Er}$  as measured by Ref. [42]. The dotted line marks the lower bound for excitation energies used in determining the dependence of  $\sigma_M^2$  on  $T$  and  $\langle J^2 \rangle$ . Its position was chosen such that at energies above this boundary, in the lightest system of  $^{16}\text{O} + ^{186}\text{Os}$ , the fission cross section dominates that of evaporations residues. As shown in (b), for heavier projectiles, the domination of fission cross sections occurs at even lower energies.

compares the fission and evaporation residue cross sections for the two reactions  $^{16}\text{O} + ^{186}\text{Os}$  [Fig. 8(a)] and  $^{34}\text{S} + ^{168}\text{Er}$  [Fig. 8(b)] [42]. The fission probabilities for  $^{24}\text{Mg} + ^{178}\text{Hf}$  are expected to lie intermediate between these reactions, but for this reaction the ER cross sections were not measured. In Fig. 8(a) it is seen that only at excitation energies above 50 MeV does the contribution from fission dominate the capture cross section. Figure 8(b) shows that for the heavier projectile, the fission cross section exceeds the evaporation residue cross section at all energies. In order to minimize deviations between the capture  $\langle J^2 \rangle$  distribution (Fig. 6) and that of the fissioning systems, an excitation energy of 50 MeV was set as the lower bound in calculating the  $\nu$  and  $\mu$  parameters. The best-fitting dependence of  $\sigma_M^2$  on  $T$  and  $\langle J^2 \rangle$ , according to Eq. (3), for the  $^{16}\text{O}$  and  $^{24}\text{Mg}$  induced reactions, was found for  $\nu = (3.54 \pm 0.05) \times 10^{-3}$  and  $\mu = (2.7 \pm 0.58) \times 10^{-7}$ . This value of  $\mu$  is much smaller than

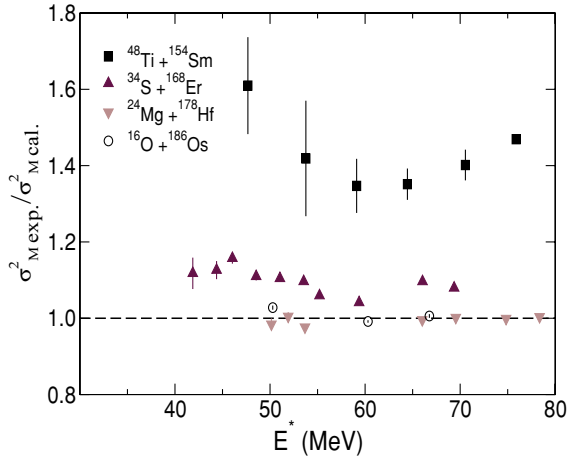


FIG. 9. (Color online) Ratio between experimental and calculated variance of the mass ratio distribution against the CN excitation energy for the four different entrance channels leading to  $^{202}\text{Po}$ .  $\sigma_{M \text{ cal}}^2$  was obtained by the application of Eq. (3) to all four systems. Since  $\nu$  and  $\mu$  parameters were obtained for CN formation, this plot measures the deviation of a given system away from CN formation. Deviations are observed for both  $^{48}\text{Ti}$  and  $^{34}\text{S}$  induced reactions.

found in the previous fit, but is consistent with the prediction of Ref. [48].

Equation (3) was then used to calculate the  $\sigma_M^2$  expected for CN formation for all four systems. Figure 9 shows the ratio between experimental ( $\sigma_{M \text{ exp}}^2$ ) and calculated ( $\sigma_{M \text{ cal}}^2$ ) variances of the fission-like fragment mass distributions, as a function of the CN excitation energy. Having used the reactions of  $^{16}\text{O} + ^{186}\text{Os}$  and  $^{24}\text{Mg} + ^{178}\text{Hf}$  to obtain the constants of Eq. (3), Fig. 9 provides a sensitive probe to measure the deviation of a given system away from the equilibrated CN reaction mechanism. The dashed line at  $\frac{\sigma_{M \text{ exp}}^2}{\sigma_{M \text{ cal}}^2} = 1$  represents the expectation for CN formation, uniformly scattered about which are the ratios for the  $^{16}\text{O}$  and  $^{24}\text{Mg}$  induced reactions at excitation energies above 50 MeV. Immediately apparent is the large deviation of the most mass-symmetric reaction,  $^{48}\text{Ti} + ^{154}\text{Sm}$ , from the line corresponding to CN formation. This deviation is strong evidence for the presence of quasifission, consistent with the mass-angle correlation shown in Fig. 4. The rise of the mass width at lower energies may be attributed to the increasing effect of deformation alignment on QF, and is addressed in the following section. A consistent, though smaller, deviation is observed in the ratio of experimental to calculated  $\sigma_M^2$  over the entire range of excitation energies for the  $^{34}\text{S}$  induced reaction. This deviation (if the result of incomplete relaxation of the mass-asymmetry) is a subtle signature of the presence of QF for the  $^{34}\text{S} + ^{168}\text{Er}$  reaction also. This deduction is consistent with the previous observation [42] of unexpectedly large angular anisotropies at sub-barrier energies.

### C. Dependence of $\sigma_M$ on $Z_p Z_t$ and $\beta_2$

It is well known that the dynamical evolution of the composite system over the multidimensional potential energy surface is strongly dependent on the  $Z_p Z_t$  of the dinuclear system,

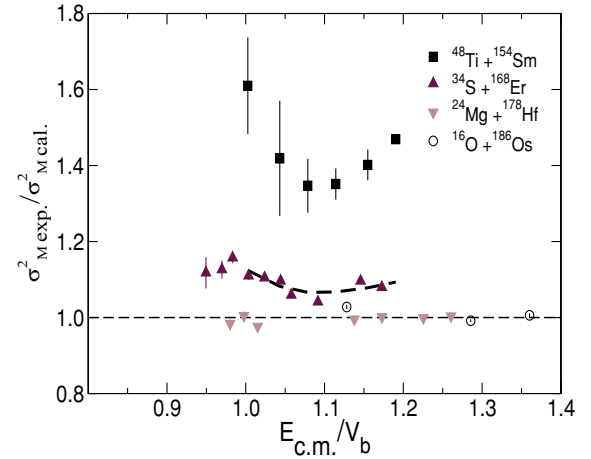


FIG. 10. (Color online)  $\frac{\sigma_M^2 \text{exp.}}{\sigma_M^2 \text{cal.}}$  values displayed are those of Fig. 9 plotted as a function of the center-of-mass energy with respect to the average capture barrier. The thick dotted line overlapping the  $^{34}\text{S} + ^{168}\text{Er}$  data points is a qualitative prediction based on scaling the  $^{48}\text{Ti} + ^{154}\text{Sm}$  data.

where  $Z_p Z_t \approx 1600$  is predicted to mark the onset of QF [7–9]. For deformed nuclei, their contact configuration at the capture barrier radius also seems to influence the trajectory of the composite system [15,24]. Consideration of the elongation of the system at contact suggests that the contact of the projectile with the sides of the target (corresponding to a higher barrier) should encourage CN formation, while an elongated contact configuration, corresponding to a lower capture barrier, will increase the probability of QF [23,24,31,49]. All target nuclei used in this experiment are statically deformed, with the static quadrupole deformation for the  $^{168}\text{Er}$  and  $^{154}\text{Sm}$  nuclei of  $\beta_2 = 0.34$  being amongst the largest of heavy nuclei.

To highlight the shape alignment effect, Fig. 10 shows the ratio of the experimental and calculated variance of the mass ratio distribution, as a function of the ratio of the center-of-mass energy to the average capture barrier. The dashed line at  $\frac{\sigma_M^2 \text{exp.}}{\sigma_M^2 \text{cal.}} = 1$  again represents the prediction for CN formation. The  $^{48}\text{Ti}$  data shows a strong rise in mass width as the energy falls toward the barrier. The thick dashed line, overlapping the  $^{34}\text{S} + ^{168}\text{Er}$  data points, is a qualitative prediction of the energy dependence for this reaction, obtained by scaling the deviation for  $^{48}\text{Ti} + ^{154}\text{Sm}$  from the CN line. The rising trend at near-barrier energies, observed for both these systems, strongly suggests that the static deformation of the target nuclei, and its alignment below-barrier, is playing a significant role in determining the probability and/or characteristics of the QF process in these reactions.

Values of  $\frac{\sigma_M^2 \text{exp.}}{\sigma_M^2 \text{cal.}}$  at  $\frac{E_{\text{c.m.}}}{V_b} = 1.1$  for all four systems, obtained using linear interpolation of adjacent points, are plotted as a function of  $Z_p Z_t$  in Fig. 11. By evaluating all data points at the same energy above the capture barrier, and normalizing to the fit which takes into account the dependence of  $\sigma_M^2$  on  $T$  and  $\langle J^2 \rangle$ , the dependence of the mass width on  $Z_p Z_t$  alone is highlighted. This shows that the increase in fission mass widths, due to the presence of QF, starts already around

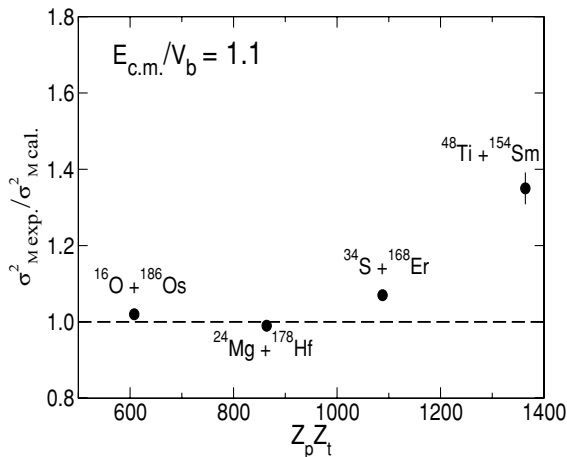


FIG. 11. Ratio of the experimental to calculated variances of the fission-like fragment mass distributions as a function of  $Z_p Z_t$  for all four reactions leading to the  $^{202}\text{Po}$  composite nucleus. The early onset of QF for the  $^{34}\text{S} + ^{168}\text{Er}$  reaction, at  $Z_p Z_t = 1088$ , is observed (see text).

$Z_p Z_t = 1000$ , while QF seems to play a dominant role by  $Z_p Z_t = 1400$ . This is seen most clearly in the strong mass-angle correlation shown in Fig. 4.

#### IV. CONCLUSIONS

Mass-angle correlations and mass ratio distributions were studied for the  $^{202}\text{Po}$  composite nucleus, produced by the reactions of  $^{16}\text{O} + ^{186}\text{Os}$ ,  $^{24}\text{Mg} + ^{178}\text{Hf}$ ,  $^{34}\text{S} + ^{168}\text{Er}$ , and  $^{48}\text{Ti} + ^{154}\text{Sm}$  at energies from the capture barriers to well above. Measurements of fission and evaporation residue cross sections were also made for the  $^{16}\text{O} + ^{186}\text{Os}$  reaction.

Simultaneous analysis, based on a generic dependence of the variance of the mass distribution on both the angular

momentum and temperature of the nucleus indicated that the  $^{16}\text{O}$  and  $^{24}\text{Mg}$  induced reactions both evolve through a true compound nucleus to fission. The fit to the data for these two lighter systems allowed prediction of the mass width for compound nucleus fission for the reactions with the heavier projectiles. The observation of much broader mass distributions than this prediction for the  $^{48}\text{Ti} + ^{154}\text{Sm}$  reaction indicates a strong contribution from quasifission. The observation of a clear mass-angle correlation for this reaction shows directly a significant probability for early reseparation of the dinuclear system, before completing a single full rotation. A slightly increased mass width was also observed at all energies for the  $^{34}\text{S} + ^{168}\text{Er}$  reaction. The smaller deviation compared to the  $^{48}\text{Ti}$  induced reaction, indicates a smaller fraction of quasifission, and/or a longer lifetime before scission. The systematics show that the  $^{34}\text{S} + ^{168}\text{Er}$  reaction marks the onset of quasifission in reactions forming  $^{202}\text{Po}$ . The role of deformation in quasifission is clearly seen through increased mass widths at near barrier energies for these two reactions.

These conclusions have only been possible through the detailed and comprehensive experimental measurements carried out in this work, making use of large area detectors covering a wide angular range. Further experiments to investigate quasifission properties will help understand the process in terms of the macroscopic variables of the compound nucleus and the entrance channel. Any dynamical model that attempts to predict the synthesis of heavy/superheavy elements should be able to describe the presence of quasifission even for such light systems.

#### ACKNOWLEDGMENTS

The authors acknowledge the financial support of an Australian Research Council Discovery grant.

- 
- [1] A. Sobiczewski *et al.*, Phys. Lett. **22**, 500 (1966).  
 [2] P. Armbruster, C. R. Phys. **4**, 571 (2003).  
 [3] K. Morita *et al.*, J. Phys. Soc. Jpn. **73**, 2593 (2004).  
 [4] Yu. Ts. Oganessian *et al.*, Nature (London) **400**, 242 (1999).  
 [5] Yu. Ts. Oganessian *et al.*, Phys. Rev. C **63**, 011301(R) (2000).  
 [6] Yu. Ts. Oganessian *et al.*, Phys. Rev. C **74**, 044602 (2006).  
 [7] W. J. Swiatecki, Phys. Scr. **24**, 113 (1981).  
 [8] S. Bjornholm and W. J. Swiatecki, Nucl. Phys. **A391**, 471 (1982).  
 [9] J. P. Blocki *et al.*, Nucl. Phys. **A459**, 145 (1986).  
 [10] P. Möller and A. J. Sierk, Nature (London) **422**, 485 (2003).  
 [11] W. U. Schröder and J. R. Huizenga, in *Damped Nuclear Reactions, Treatise on Heavy-ion Science*, edited by D. A. Bromley (Plenum Press, New York, 1984), Vol. 2, p. 115.  
 [12] J. Toke *et al.*, Nucl. Phys. **A440**, 327 (1985).  
 [13] B. B. Back *et al.*, Phys. Rev. C **53**, 1734 (1996).  
 [14] D. J. Hinde *et al.*, J. Nucl. Radiochem. Sci. **3**, 31 (2002).  
 [15] S. Mitsuoka, H. Ikezoe, K. Nishio, K. Satou, and J. Lu, Phys. Rev. C **65**, 054608 (2002).  
 [16] G. N. Knyazheva *et al.*, Phys. Rev. C **75**, 064602 (2007).  
 [17] R. Bock *et al.*, Nucl. Phys. **A388**, 334 (1982).  
 [18] W. Q. Shen *et al.*, Phys. Rev. C **36**, 115 (1987).  
 [19] M. F. Rivet *et al.*, Z. Phys. A **330**, 295 (1988).  
 [20] B. B. Back *et al.*, Phys. Rev. Lett. **50**, 818 (1983).  
 [21] B. B. Back *et al.*, Phys. Rev. C **32**, 195 (1985).  
 [22] R. Vandenbosch and J. R. Huizenga, *Nuclear Fission* (Academic, New York, 1973).  
 [23] D. J. Hinde *et al.*, Phys. Rev. Lett. **74**, 1295 (1995).  
 [24] D. J. Hinde, M. Dasgupta, J. R. Leigh, J. C. Mein, C. R. Morton, J. O. Newton, and H. Timmers, Phys. Rev. C **53**, 1290 (1996).  
 [25] J. C. Mein, D. J. Hinde, M. Dasgupta, J. R. Leigh, J. O. Newton, and H. Timmers, Phys. Rev. C **55**, R995 (1997).  
 [26] J. P. Lestone *et al.*, J. Phys. G **23**, 1349 (1997).  
 [27] K. Nishio *et al.*, Phys. Rev. Lett. **93**, 162701 (2004).  
 [28] S. Mitsuoka, H. Ikezoe, K. Nishio, and J. Lu, Phys. Rev. C **62**, 054603 (2000).  
 [29] A. C. Berriman *et al.*, Nature (London) **413**, 144 (2001).  
 [30] A. Yu. Chizhov *et al.*, Phys. Rev. C **67**, 011603(R) (2003).  
 [31] D. J. Hinde, M. Dasgupta, and A. Mukherjee, Phys. Rev. Lett. **89**, 282701 (2002).

- [32] R. G. Thomas *et al.*, Phys. Rev. submitted.
- [33] S. Raman *et al.*, At. Data Nucl. Data Tables **78**, 1 (2001).
- [34] J. R. Leigh *et al.*, Phys. Rev. C **52**, 3151 (1995).
- [35] D. J. Hinde, D. Hilscher, H. Rossner, B. Gebauer, M. Lehmann, and M. Wilpert, Phys. Rev. C **45**, 1229 (1992).
- [36] C. Lebrun *et al.*, Nucl. Phys. **A321**, 207 (1979).
- [37] M. E. Faber, Phys. Rev. C **24**, 1047 (1981).
- [38] B. G. Glagola, B. B. Back, and R. R. Betts, Phys. Rev. C **29**, 486 (1984).
- [39] M. G. Itkis and A. Ya. Rusanov, Phys. Part. Nuclei **29**, 160 (1998).
- [40] A. B. Balantekin, A. J. DeWeerd, and S. Kuyucak, Phys. Rev. C **54**, 1853 (1996).
- [41] K. Hagino *et al.*, Comput. Phys. Commun. **123**, 143 (1999).
- [42] C. R. Morton, A. C. Berriman, R. D. Butt, M. Dasgupta, A. Godley, D. J. Hinde, and J. O. Newton, Phys. Rev. C **62**, 024607 (2000).
- [43] J. O. Newton, R. D. Butt, M. Dasgupta, D. J. Hinde, I. I. Gontchar, C. R. Morton, and K. Hagino, Phys. Rev. C **70**, 024605 (2004).
- [44] A. J. Sierk, Phys. Rev. C **33**, 2039 (1986).
- [45] D. J. Hinde, A. C. Berriman, M. Dasgupta, J. R. Leigh, J. C. Mein, C. R. Morton, and J. O. Newton, Phys. Rev. C **60**, 054602 (1999).
- [46] A. Saxena *et al.*, Phys. Rev. C **49**, 932 (1994).
- [47] D. Marquardt, J. Appl. Math. **11**, 431 (1963).
- [48] G. D. Adeev *et al.*, Phys. Part. Nuclei **19**, 1229 (1988).
- [49] V. Yu. Denisov *et al.*, Eur. Phys. J. A **15**, 375 (2002).